**H1prelim-11-032** submitted to

**XIX International Workshop on Deep-Inelastic Scattering and Related Subjects (DIS2011)** April 11-15, 2011, Newport News, VA USA
Parallel Session: **QCD and Final States**

Electronic Access: *www-h1.desy.de/publications/H1preliminary.short.list.html*

# Measurement of Multijet Production in Deep-Inelastic $ep$ Scattering at High $Q^2$ and Determination of $\alpha_s(M_Z)$

H1 Collaboration

**Abstract**

Inclusive jet, dijet and trijet differential cross sections have been measured in neutral current deep-inelastic scattering for exchanged boson virtualities $150 < Q^2 < 15000\,\mathrm{GeV}^2$ with the H1 detector at HERA using an integrated luminosity of $351\,\mathrm{pb}^{-1}$. The multijet cross sections are presented as a function of $Q^2$, the transverse momentum of the jet $P_{\mathrm{T}}$ (the mean transverse momentum for dijets and trijets) in the Breit frame and the proton's longitudinal momentum fraction of the parton participating in the hard interaction $\xi$. The cross sections are compared to perturbative QCD calculations in next-to-leading order and subsequently used to determine the value of the strong coupling $\alpha_s(M_Z)$.

# 1 Introduction

Jet production in neutral current (NC) deep-inelastic scattering (DIS) at HERA provides an important testing ground for Quantum Chromodynamics (QCD). While inclusive DIS gives only indirect information on the strong coupling via scaling violations of the proton structure functions, the production of jets in the Breit frame is directly sensitive to $\alpha_s$. Thus, in the extraction of Parton Distribution Functions (PDFs) using inclusive DIS data, the inclusion of jet production can provide an important constraint.

The Born level contribution to DIS generates no transverse momentum in the Breit frame, where the virtual boson and the proton collide head on. Significant transverse momentum $P_{\mathrm{T}}$ in the Breit frame is produced at leading order (LO) in the strong coupling $\alpha_s$ by the QCD-Compton and boson-gluon fusion processes. In LO the proton's momentum fraction carried by the emerging parton is given by $\xi = x_{\mathrm{Bj}}(1 + M_{12}^2/Q^2)$, where $x_{\mathrm{Bj}}$ denotes the Bjorken scaling variable, $M_{12}$ the invariant mass of the two jets of highest $P_{\mathrm{T}}$, and $Q^2$ the negative four momentum transfer squared. In case of the trijet measurement, $M_{12}$ is replaced by the invariant mass of the three jets of highest $P_{\mathrm{T}}$ in the definition of $\xi$. In the kinematical regions of low $Q^2$, low $P_{\mathrm{T}}$ and low $\xi$, boson-gluon fusion dominates jet production and provides direct sensitivity to $\alpha_s \otimes g$, i.e. the gluon component of the PDFs and $\alpha_s$. At high $Q^2$ and high $P_{\mathrm{T}}$ QCD-Compton processes are dominant, which are sensitive to the valence quark distributions and $\alpha_s$. Thus, in the extraction of PDFs the inclusion of jet production can provide an important constraint on $\alpha_s$ and allows to disentangle the correlation between $\alpha_s$ and the gluon [1, 2].

In a previous publication on multi-jet production at high $Q^2$ by the H1 collaboration [3] measurements of normalised multi-jet cross sections and extractions of $\alpha_s(M_Z)$ have been made using HERA-1 and HERA-2 data. In the analyses reported here, improvements in the reconstruction of tracks and calorimetric energy have entered. A new calibration of the hadronic energy as measured by the H1 liquid argon (LAr) calorimeter and the tracks in the tracking detector has lead to a better jet energy resolution and a jet energy scale uncertainty of $1\%$. These improvements allowed to extend the pseudorapidity of the measured jets in the proton direction from $2.0$ to $2.5$ and in the photon direction from $-0.8$ to $-1.0$. Due to the corresponding increase in statistics also the trijet cross section can be measured double differentially in $Q^2$, $P_{\mathrm{T}}$ and $Q^2$, $\xi$.

In the analyses presented here HERA-2 data with an integrated luminosity of 351 pb$^{-1}$ have been used, yielding for the first time results on double-differential dijet and trijet cross sections. The single and double differential measurements of inclusive jet cross sections can be directly compared to the previous measurements of inclusive jet production at high $Q^2$ published by the H1 collaboration [4] using HERA-1 data. The inclusive jet measurement presented here is performed in the same phase space, but has significantly reduced uncertainties due to the improvements in the reconstruction and much larger statistics. The measurements are compared with QCD predictions at next-to-leading order (NLO) corrected for hadronisation effects. Values of $\alpha_s$ are extracted from fits of the predictions to the new multi-jet cross sections.

## 2 Event Selection and Jet Phase Space

The NC DIS events, which are primarily selected by requiring a scattered electron, have to fulfill the following requirements:

$$150 < Q^2 < 15000\,\mathrm{GeV}^2 \quad \text{and} \quad 0.2 < y < 0.7\,,$$

with $Q^2$ referring to the virtuality of the exchanged vector boson ($\gamma$ and $\mathrm{Z}^0$) and $y = Q^2/(s\,x_{\mathrm{Bj}})$ to the inelasticity of the interaction. The $ep$ centre-of-mass energy squared is given by $s \simeq 4E_eE_p$, where $E_e$ and $E_p$ are the incident electron (or positron) and proton beam energies of $27.5$ and $920\,\mathrm{GeV}$ in the HERA laboratory frame. The variable $x_{\mathrm{Bj}}$ refers to the Bjorken scaling variable. The two variables $Q^2$ and $y$ are reconstructed from the four momenta of the scattered electron and the hadronic final state particles using the electron-sigma method [5]. The selection of events passing the above cuts provides the NC DIS sample, which forms the basis of the subsequent jet analysis.

The jet finding is performed in the Breit frame, where the boost from the laboratory system is determined by $Q^2$, $y$ and by the azimuthal angle $\phi_e$ of the scattered electron. Particles of the hadronic final state (HFS) are clustered into jets using the inclusive $k_{\mathrm{T}}$ algorithm [6] as implemented in FastJet [7], with the massless $P_{\mathrm{T}}$ recombination scheme and with the distance parameter $R_0 = 1$. The requirement

$$-1.0 < \eta_{\mathrm{lab}} < 2.5$$

where $\eta_{\mathrm{lab}}$ is the jet pseudorapidity in the laboratory frame, is imposed on all jets and ensures that jets are contained within the acceptance of the LAr calorimeter and are well calibrated. Jets are ordered according to decreasing transverse momentum $P_{\mathrm{T}}$ in the Breit frame. For massless jets $P_{\mathrm{T}}$ is identical to the transverse energy $E_{\mathrm{T}}$. The jet with the highest $P_{\mathrm{T}}$ is referred to as the leading jet. Every jet with transverse momentum $P_{\mathrm{T}}$ in the Breit frame satisfying

$$7 < P_{\mathrm{T}} < 50\,\mathrm{GeV}$$

contributes to the inclusive jet cross section. Events with at least two (three) jets with transverse momentum larger than 5 GeV are considered as dijet (trijet) events. In order to avoid regions of phase-space where fixed order perturbation theory is not reliable [8], dijet events are accepted only if the invariant mass $M_{12}$ of the two leading jets exceeds 16 GeV. The same requirement, $M_{12} > 16\,\mathrm{GeV}$, is applied to the trijet events so that the trijet sample is a subset of the dijet sample. In summary, the requirements for dijets and trijets are:

$$5 < P_{\mathrm{T}} < 50\,\mathrm{GeV} \quad \text{and} \quad M_{12} > 16\,\mathrm{GeV}\,.$$

## 3 Definition of the observables

The measurements presented refer to the phase-space given above and in table 1. Inclusive jet cross sections are measured as functions of $Q^2$ and the transverse jet momentum $P_{\mathrm{T}}$ in the Breit frame. Dijet and trijet cross sections are measured as function of $Q^2$, the average transverse momentum $\langle P_{\mathrm{T}}\rangle = \frac{1}{N}\sum_i^N P_{\mathrm{T}}^{\mathrm{jet},i}$, with $N = 2$ ($N = 3$) for the dijet (trijet) case and as function of the proton momentum fraction $\xi$. All jet cross sections are presented single and double differentially in these variables.

# 4 Detector corrections

The following leading order (LO) Monte Carlo (MC) event generators are used for the correction procedure: DJANGOH [9], which uses the Colour Dipole Model with QCD matrix element corrections as implemented in ARIADNE [10], and RAPGAP [11], based on QCD matrix elements matched with parton showers in leading log approximation. In both MC generators the hadronisation is modelled with Lund string fragmentation [12]. All generated events are passed through a GEANT3 [13] based simulation of the H1 apparatus, using an accurate and fast parametrisation of electromagnetic showers for the simulation of calorimetric energy deposits [14–17]. The simulated events are then reconstructed using the same program chain as for the data. Both RAPGAP and DJANGOH provide a good overall description of the inclusive DIS sample. To further improve the agreement between MC and data for the jet samples, the jet multiplicities are weighted as a function of $Q^2$ in the Monte Carlo simulations. Additionally, the MC events are weighted as function of $P_{\mathrm{T}}$ and $\eta$ of the most forward jet in the Breit frame [18]. After weighting, the simulations provide a good description of the shapes and normalisation of all data distributions. Examples are shown for the NC DIS sample in figure 1 and for the inclusive, dijet and trijet samples in figures 2, 3 and 4, respectively.

The bins in $Q^2$, $P_{\mathrm{T}}$ and $\xi$ used to measure the jet cross sections are given in table 2. The associated bin purities, defined as the fraction of the events reconstructed in a particular bin that originate from that bin on the generator level, are typically $50 - 60\%$ and always greater than $40\%$. The correction factors deviate typically by less than $20\%$ from unity. Arithmetic means of the correction factors determined from the reweighted RAPGAP and DJANGOH event samples are used and half of the difference is assigned as a model uncertainty.

The above correction factors include QED radiation and electroweak effects. The effects of QED radiation, which are typically $5\%$, are corrected for by means of the HERACLES [19] program. The LEPTO event generator [20] is used to correct the $e^+p$ and $e^-p$ data for their different electroweak effects. The resulting pure photon exchange cross sections obtained from $e^+p$ and $e^-p$ data samples are then averaged.

## 4.1 Experimental uncertainties

Due to a large effort by the H1 collaboration improvements on all aspects of the reconstruction of the final state could be achieved. Most notably, the main experimental uncertainties of the jet measurement, which are related to the measurement of the HFS and the scattered electron, could be reduced. This leads to much reduced experimental uncertainties on the jet cross sections with respect to previous jet measurements by the H1 collaboration. All systematic uncertainties of the jet observables are determined by propagating the corresponding estimated measurement errors through the full analysis.

### 4.1.1 Hadronic Energy Scale

For the reconstruction of the HFS an energy-flow algorithm has been used by the H1 collaboration, which combines information from tracking and calorimetric measurements. A detailed description of the employed track detectors and the LAr calorimeter can be found elsewhere [21].

Recently, a large effort was undertaken to improve on all aspects of the reconstruction of the HFS. The track and vertex reconstruction was improved by using a double-helix trajectory for the track fits, which can take into account secondary scatterings inside the detector material. The calorimetric measurement benefitted from a separation of hadronic and electromagnetic showers based on shower shape estimators and neural networks [18].

Based on these improvements a new calibration method for the HFS was developed, allowing the calibration of individual calorimetric energy deposits, depending on their composition of hadronic and electromagnetic components [18]. Due to the over-constrained kinematics at HERA, the double-angle method [5] can be used to predict the transverse momentum of the HFS, $P_{\mathrm{T}}^{\mathrm{da}}$. This can be exploited using a dedicated sample, consisting of quark parton model-type processes, where a single jet balances the scattered electron in transverse momentum. In this sample the measurement of $P_{\mathrm{T}}^{\mathrm{da}}$ is not influenced by initial or final state radiation or by losses due to the limited detector acceptance. It can thus be used to derive calibration constants for the energy reconstruction and for stringent tests of the jet energy scale uncertainty. Figure 5 shows the mean value of the ratio of $P_{\mathrm{T}}^{\mathrm{h}}$, which is the calibrated transverse momentum of the HFS, to $P_{\mathrm{T}}^{\mathrm{da}}$. The variable $P_{\mathrm{T}}^{\mathrm{da}}$ is independent of the calibration and is used as a reference scale in both, data and MC simulations. The reconstruction of the absolute energy scale is achieved within $2\%$. At the bottom of figure 5 the double-ratio of data to MC is shown. A jet energy scale uncertainty of $1\%$ is achieved over the full accessible range of jet energy $E_{\mathrm{jet}}$ and pseudorapidity $\eta_{\mathrm{jet}}$. Also shown in figure 5 are the mean values of the $P_{\mathrm{T}}$-balance distributions as function of the electromagnetic energy fraction of the jet, $f_{\mathrm{em,jet}}$, which is calculated using the developed separation of electromagnetic and hadronic showers in the LAr calorimeter. The $P_{\mathrm{T}}$-balance exhibits a flat response within $2\%$ as function of $f_{\mathrm{em,jet}}$ and is also described within $1\%$ by the MC simulations. The hadronic energy scale uncertainty of $1\%$ results in errors between $2\%$ at low $P_{\mathrm{T}}$ and $5\%$ at high $P_{\mathrm{T}}$ on the jet cross section measurement.

#### 4.1.2 Electron Reconstruction

The scattered electron is measured in the LAr calorimeter. The relative uncertainty of the electron energy calibration is $0.5\%$ and increases to $1\%$ for electrons in the forward direction. The absolute uncertainty of the electron polar angle is 1 mrad. The uncertainty on the electron identification efficiency is $0.5\%$ in the central region of the detector and $2\%$ in the forward region. Uncertainties in the electron reconstruction affect the event kinematics and thus the boost to the Breit frame. This in turn leads to a relative error on the jet cross sections of $1\%$ in the bulk of the phase space and up to $2\%$ in the highest $Q^2$ region.

#### 4.1.3 Model Dependence

The model dependence of the detector correction factors is estimated as described in section 4. It reflects the sensitivity of the detector simulation to the details of the model, especially the parton showering, and their impact on the migration into the selected samples and between adjacent bins in $P_{\mathrm{T}}$ within the sample. The model dependence ranges typically from $2\%$ to $4\%$ for the inclusive and dijet measurements and between $4\%$ and $10\%$ for the trijet measurements.

### 4.1.4 Background Subtraction

The background is estimated using MC predictions for photoproduction, QED Compton scattering, low $Q^2$ NC DIS and dilepton production. The total background in the NC DIS and inclusive jet samples amounts to $1.2\%$ and $1.1\%$, respectively. The estimated uncertainty due to the background subtraction is in all bins smaller than $0.5\%$. The background in the dijet and trijet samples is negligible.

### 4.1.5 Normalisation Uncertainties

The uncertainties of the luminosity measurement, the trigger efficiency and the vertex-finding efficiency amount to about $3\%$ when added in quadrature and are independent of $Q^2$ or $P_{\mathrm{T}}$.

### 4.1.6 Summary of experimental uncertainties

The two dominant experimental errors on the jet cross sections arise from the uncertainty on the hadronic energy scale and the model dependence of the data correction. The uncertainty due to the model dependence exceeds the former in case of the trijet measurement. The overall experimental error, calculated as the quadratic sum of all the contributions inventoried above, ranges typically between $4\%$ and $6\%$ and increases up to $15\%$ in the regions of highest $P_{\mathrm{T}}$ or $Q^2$ where it is dominated by statistical uncertainties.

# 5 NLO QCD prediction of jet cross sections

Reliable quantitative predictions of jet cross sections in DIS require the perturbative calculations to be performed at least to NLO in the strong coupling. By using the inclusive $k_T$ jet algorithm with radius parameter $R_0 = 1$, the observables used in the present analysis are infrared and collinear safe, and the non-perturbative effects are expected to be small [2]. In addition, applying this algorithm in the Breit frame has the advantage that initial state singularities can be absorbed in the definition of the PDFs [22].

Jet cross sections are predicted at the parton level using the same jet definition as in the data analysis. The QCD predictions for the jet cross sections are calculated using the NLOJET++ program at NLO in the strong coupling [23, 24]. When comparing data and theory predictions the strong coupling at the $Z^0$ boson mass is taken to be $\alpha_s(M_Z) = 0.118$ and is evolved as a function of the renormalisation scale with two loop precision. The calculations are performed in the $\overline{MS}$ scheme for five massless quark flavours. The PDFs of the proton are taken from the HERAPDF1.5 set [25]. The factorisation and renormalisation scales are set to $\mu_{\mathrm{f}} = \mu_{\mathrm{r}} = \sqrt{(P_{\mathrm{T}}^2 + Q^2)/2}$, where $\langle P_{\mathrm{T}} \rangle$ is used instead of $P_{\mathrm{T}}$ in the case of the dijet and trijet measurements. This choice of the renormalisation scale is motivated by the presence of two hard scales, $P_{\mathrm{T}}$ and $Q^2$, in jet production in DIS. No QED radiation or $Z^0$ exchange is included in the calculations, but the running of the electromagnetic coupling with $Q^2$ is taken into account.

Hadronisation corrections are calculated for each bin using MC event generators. These corrections are determined as the ratio of the cross section at the hadron level to the cross section at the parton level after parton showers. They typically differ by less than $10\%$ from unity and are obtained using the event generators DJANGOH and RAPGAP, which agree to within $2\%$ to $4\%$. The arithmetic means of the two Monte Carlo hadronisation correction factors are used, while the full difference is considered as systematic error.

The dominant theoretical error is due to the uncertainty related to the neglected higher orders in the perturbative calculation. The accuracy of the NLO calculation is conventionally estimated by separately varying the chosen scales for $\mu_{\rm f}$ and $\mu_{\rm r}$ by arbitrary factors of typically $0.5$ and 2. At high transverse momentum, above 30 GeV, the perturbative QCD (pQCD) calculations do not depend monotonically on $\mu_{\rm r}$ in some $Q^2$ bins. In such cases, the difference between the maximum and minimum cross sections found in the variation interval is taken, in order not to underestimate the scale dependence. Renormalisation and factorisation scale uncertainties are added in quadrature, the former outweighing the latter by a factor of two on average.

# 6 Results

In the following, the single and double differential cross sections are presented for inclusive jet, dijet and trijet production at the hadron level. The measured observables are presented in figures 6 to 13. The results are shown together with their experimental uncertainties and are compared to NLO predictions, corrected for hadronisation effects and effects from $Z^0$ exchange. These measurements are subsequently used to extract the strong coupling $\alpha_s(M_Z)$ as shown in table 3 and figures 17 to 19.

## 6.1 Cross section measurements compared to NLO predictions

The inclusive jet cross sections as a function of $Q^2$ and $P_{\rm T}$ are shown in figure 6 together with the NLO predictions. The double differential results as a function of $P_{\rm T}$ in six ranges of $Q^2$ are shown in figure 7. Dijet cross sections as a function of $Q^2$, $\langle P_{\rm T}\rangle$ and $\xi$ and their comparison to NLO are shown in figure 8, while the double differential cross sections are presented as function of $\langle P_{\rm T}\rangle$ and $\xi$ in six different ranges of $Q^2$ in figures 9 and 10. The trijet cross sections are presented single differentially in figure 11 and double differentially in figures 12 and 13. The ratios of the inclusive jet, dijet and trijet measurements to the NLO calculations are shown in figures 14 to 16, where they are compared to NLO predictions using different proton PDFs.

The new measurement of the inclusive jet cross section (figures 6 and 7) is compatible with a previous measurement [4] of the H1 collaboration using HERA-1 data [18]. The precision is improved by typically a factor of two to three, which is mainly due to the higher statistics and the improved hadronic energy scale uncertainty from previously $2\%$ to now $1\%$. The QCD NLO predictions for all inclusive jet cross sections provide a good description of the data over the whole phase space. In almost all bins the theory error, dominated by the $\mu_{\rm r}$ scale uncertainty, is significantly larger than the total experimental uncertainty, which is dominated by the uncertainty due to the model dependence of the data correction and the hadronic energy scale uncertainty.

The dijet cross sections are presented single differentially in figure 8. The data show the tendency to lie below the NLO predictions, being at the lower edge of the theory uncertainty. This is mainly due to the region of small mean transverse momentum, $7 < \langle P_{\rm T} \rangle < 11\,{\rm GeV}$, as can be observed in figure 8b. The double differential dijet cross sections are presented in figures 9 and 10. It can be seen in figure 9 that at small $\langle P_{\rm T} \rangle$ the NLO predictions are about $10\%$ higher than the data, indicating a preference for a smaller value of $\alpha_s(M_Z)$ than 0.118. In general the agreement with the NLO predictions is good over the whole phase space. The double differential dijet cross sections as function of $Q^2$ and $\xi$ are presented in figure 10. Kinematic constraints due to the required jet transverse momenta, as well as the demand of a minimal invariant mass $M_{12}$ of the two jets, leads to a reduction of the cross section at small values of $\xi$. At large values of $\xi$ the decreasing quark and gluon densities lead to a decrease of the cross section. The cross section has a maximum at small values of $\xi$ at low $Q^2$, which shifts to higher values as $Q^2$ increases with the inelasticity $y$ remaining in a fixed range. The different phase space of the dijet measurement with respect to a recent measurement by the ZEUS collaboration [26] prevents a direct comparison, but the experimental uncertainties are comparable.

The trijet cross sections are already at the Born level proportional to $\mathcal{O}(\alpha_s^2)$ and the NLO calculations include terms of $\mathcal{O}(\alpha_s^3)$. This means that already at LO the triple gluon vertex contributes to the cross section, while the four gluon vertex is included in the NLO calculation. The trijet cross sections thus provide an important test of pQCD and the running of the strong coupling. The trijet cross sections, measured single differentially as function of $Q^2$, $\langle P_{\rm T} \rangle$ and $\xi$, are shown in figure 11. The experimental uncertainties are larger than in the dijet case, due to a larger uncertainty of the model dependence. The measured trijet cross sections have uncertainties of 6% to 7% at low $Q^2$ and low $\langle P_{\rm T} \rangle$, which are a factor of about two smaller than the theoretical uncertainties, which are a factor of about 1.5 larger than in the dijet case. At high $Q^2$, high $\langle P_{\rm T} \rangle$ and high $\xi$ the experimental uncertainties increase because of a larger model dependence and the increasing uncertainty due to the hadronic energy scale, whereas the theoretical uncertainties decrease. In these regions the theoretical and experimental uncertainties of the trijet cross sections become comparable. The double differential trijet cross sections measured as function of $Q^2$ and $\langle P_{\rm T} \rangle$ and $Q^2$ and $\xi$ are presented in figures 12 and 13. These are the first measurements of double differential trijet cross sections in NC DIS at high $Q^2$. They show a similar behaviour as the dijet cross sections, but are about five times smaller. The cross section as function of $\xi$ is shifted towards larger values of $\xi$, due to the higher invariant mass of the trijet system compared to that of the dijet system. The experimental uncertainties are to a large part dominated by the model dependence. They are about 7% at small values of $\langle P_{\rm T} \rangle$ and $\xi$ and between 10–15% at large values of these variables. The uncertainties on the theoretical predictions are between 10–15%, with smaller uncertainties at high $Q^2$ and $\langle P_{\rm T} \rangle$ and larger uncertainties at small $Q^2$ and $\langle P_{\rm T} \rangle$. The data are well described by the NLO calculations over the full phase space of the measurement.

In figures 14 to 16 the ratios of NLO calculations, using different PDF parametrisations, to the measured double differential cross sections are presented as function of $P_{\rm T}$ ($\langle P_{\rm T} \rangle$ in case of the dijet and trijet measurements) in bins of $Q^2$. The theoretical uncertainty related to the variations of the renormalisation and factorisation scales are shown together with the predictions using HERAPDF1.5. Also shown are the central values of predictions using the CT10 [27] and

NNPDF2.0 [28] parametrisations of the proton PDFs. Differences in the predicted jet cross sections of the order of $4-8\%$ can be observed. In the dijet case the observed differences are largest, and the theoretical uncertainties are smaller than in the case of the inclusive jet or trijet measurements. Therefore the dijet cross sections will provide the most stringent constraints when included in PDF determinations. In the inclusive jet (figure 14) and dijet case (figure 15) it can be observed that the predictions obtained with the CT10 and NNPDF2.0 parametrisations describe the data better at low $Q^2$ and low $P_{\mathrm{T}}$ than the ones using HERAPDF1.5, which can be attributed to differences in the gluon distribution. At high $Q^2$ and high $P_{\mathrm{T}}$, where QCD-Compton processes dominate the cross section, the NLO predictions using HERAPDF1.5 provide a better description of the data. In figure 16 the ratio of NLO predictions to the measured trijet cross sections are shown, where only small differences between the predictions using different PDF parametrisations can be observed. The trijet cross sections are not expected to have a large impact in determining the gluon or valence quark distributions, but will however provide an important constraint on $\alpha_s$.

## 6.2 Extraction of the strong coupling

The QCD predictions for jet production depend on $\alpha_s$ and on the parton density functions of the proton. The strong coupling $\alpha_s$ is determined from the measured jet cross sections using the CT10 proton PDFs. Besides other data and Tevatron jet data only HERA-1 data were used to obtain these parametrisations, which makes them independent of the present jet measurements.

While the calculations of jet cross sections in NLO can take considerable time, the FASTNLO program [29] provides an efficient method to calculate these cross sections. It is based on matrix elements from NLOJET++ and convolutes them with the PDFs and $\alpha_s(\mu_{\mathrm{r}})$, where the latter is obtained using the two-loop solution of the renormalisation group equation. The program includes a coherent treatment of the renormalisation and factorisation scale dependencies of all ingredients to the cross section calculation. The obtained NLO predictions are corrected for hadronisation effects and effects due to $Z^0$ exchange as described in section 5.

The extraction of $\alpha_s(M_Z)$ is performed with fits based on a $\chi^2$-minimisation using the Hessian method [30]. This method takes into account correlations of experimental uncertainties and has already been used in global data analyses [30,31] and in previous H1 publications [3,4,32]. Parameters representing correlated systematic shifts of detector related observables are left free in the fit. The experimental uncertainty on the obtained value of $\alpha_s(M_Z)$ is defined by the change in $\alpha_s(M_Z)$ which gives an increase in $\chi^2$ of one unit with respect to the minimal value.

The correlations of the experimental uncertainties between data points have been estimated as follows:

- The statistical correlations between different $P_{\mathrm{T}}$ bins in case of the inclusive jet measurement are taken into account via a correlation matrix obtained from the data.
- The uncertainty of the LAr electron and hadronic energy scale is equally shared between correlated and uncorrelated contributions [3,4].
- The measurement of the electron polar angle is assumed to be fully correlated [33].

- The model dependence of the experimental correction factors is considered as fully uncorrelated after the averaging procedure described in section 4.1.
- The uncertainties connected with the luminosity measurement, the electron and vertex reconstruction efficiency and the trigger efficiency are taken to be fully correlated.

The impact on the $\alpha_s$ determination of the sharing of correlated and uncorrelated contributions between the different sources of uncertainty has been investigated by changing the assumptions on the HFS and electron energy scales and the electron polar angle to fully correlated or uncorrelated. The fitted value of $\alpha_s$ varies by less than $0.2\%$ and the estimated uncertainty by less than $0.1\%$ of $\alpha_s$.

The theory error is estimated by the so called *offset* method as the difference between the value of $\alpha_s$ from the nominal fit to the value when the fit is repeated with independent variations of different sources of theoretical uncertainties as described in section 5. The resulting uncertainties due to the different sources are summed in quadrature. The up (or down) variations are applied simultaneously to all bins in the fit. The impact of the hadronisation corrections on $\alpha_s$ is between $0.4\%$ and $1.0\%$, while that of the factorisation scale amounts to $0.5\%$. The largest uncertainty, of typically $3\%$ to $4\%$, corresponds to the missing higher orders in the NLO calculations, estimated by varying the renormalisation scale as described in section 5.

The uncertainty on $\alpha_s$ due to the used PDFs is estimated by propagating the CT10 uncertainties with the offset method. The up and down variations of the calculated cross sections are estimated using the CT10 eigenvalues using the prescription given in [34]. The typical size of the resulting error is $1.7\%$ for $\alpha_s$ from the inclusive jet or dijet cross sections and $0.8\%$ for $\alpha_s$ from the trijet cross sections. The PDFs also depend on the value of $\alpha_s(M_Z)$ assumed in the PDF determination. To test for such a potential bias, the fits were repeated with CT10 PDFs obtained with different values of $\alpha_s(M_Z)$ in the range of $0.113$–$0.123$. The resulting change in the obtained values of $\alpha_s(M_Z)$ was found to be well within the uncertainties attributed to the PDF uncertainty.

The obtained values of $\alpha_s(M_Z)$ using the double differential inclusive jet, dijet and trijet cross sections as function of $P_{\rm T}$ (or $\langle P_{\rm T}\rangle$) are:

$$\begin{aligned}
\text{inc. jet} : \alpha_s(M_Z) &= 0.1190 \pm 0.0021\,(\text{exp.}) \pm 0.0020\,(\text{pdf})\,{}^{+0.0050}_{-0.0056}\,(\text{th.})\\
\text{dijet} : \alpha_s(M_Z) &= 0.1146 \pm 0.0022\,(\text{exp.}) \pm 0.0021\,(\text{pdf})\,{}^{+0.0044}_{-0.0045}\,(\text{th.})\\
\text{trijet} : \alpha_s(M_Z) &= 0.1196 \pm 0.0016\,(\text{exp.}) \pm 0.0010\,(\text{pdf})\,{}^{+0.0055}_{-0.0039}\,(\text{th.})
\end{aligned}$$

which are compatible within the uncertainties. These values are consistent with previously determined values of $\alpha_s(M_Z)$ by H1 [3, 4, 35] and the world average [36]. In each of these fits the shifts in the electron energy scale, electron polar angle, normalisation uncertainties and the hadronic final state energy scale are found to be consistent with the a priori estimated uncertainties. The obtained values of $\chi^2$ per degrees of freedom are above but near unity and are given in table 3. The experimental uncertainties are somewhat larger than in a recent determination of $\alpha_s(M_Z)$ from high $Q^2$ jet data by the H1 collaboration, where normalised jet cross sections have been used. This leads to smaller experimental uncertainties, since all normalisation uncertainties cancel in the ratio. In the case of the $\alpha_s$ extraction from inclusive jet and dijet data, the normalisation uncertainties give the largest contribution to the experimental uncertainty. In the trijet case the experimental uncertainty is smallest, since the cross section is $\mathcal{O}(\alpha_s^2)$ already in LO and, therefore, more sensitive to the slope of the cross section and less affected by the overall normalisation of the data. Also in the trijet case, the value of $\alpha_s(M_Z)$ has the smallest PDF uncertainty. In all cases the theoretical uncertainties, which are dominated by uncertainties due to missing higher orders, are larger by about a factor of two than the experimental and PDF uncertainties.

Individual fits of $\alpha_s(M_Z)$ are made to each of the $24$ measurements of the double differential inclusive jet and dijet cross sections and to the $17$ points of the trijet measurement, as shown in figures 17 to 19. The values of $\alpha_s(M_Z)$ from the individual determinations are obtained by considering only the uncorrelated uncertainty of every measured data point. All obtained values of $\alpha_s(M_Z)$ agree within the uncertainties. No systematic shift from the combined value is observed, which would indicate a bias coming from one of the correlated uncertainties.

# 7 Conclusion

Measurements of the inclusive jet, dijet and trjet cross sections in the Breit frame in NC DIS in the range $150 < Q^2 < 15000\,\mathrm{GeV}^2$ and $0.2 < y < 0.7$ using H1 data taken during the HERA-2 running are presented. The obtained jet cross sections benefit significantly from recent improvements in the reconstruction of the hadronic final state and have uncertainties of only $4-8\%$ on average. The double differential trijet cross sections are measured for the first time in NC DIS at high $Q^2$.

Calculations at NLO QCD, corrected for effects from hadronisation and $Z^0$ exchange, provide a good description of the single and double differential cross sections as functions of the jet transverse momentum $P_\mathrm{T}$, the boson virtuality $Q^2$ as well as the proton momentum fraction $\xi$. The value of the strong coupling $\alpha_s(M_Z)$ is determined from fits of the NLO predictions to the measured jet cross sections. The experimentally most precise determination of $\alpha_s(M_Z)$ is obtained by using the double differential trijet cross sections. It reaches the highest sensitivity to $\alpha_s$ and is least affected by the correlated normalisation uncertainties. The value of $\alpha_s(M_Z)$ determined from the trijet cross sections also shows the smallest uncertainty due to the proton PDF parametrisation uncertainty.

The dominating source of uncertainty in the determination of $\alpha_s(M_Z)$ is due to the renormalisation scale dependence, which is used to estimate the effect of missing higher orders beyond NLO in the pQCD prediction.

# Acknowledgements

We are grateful to the HERA machine group whose outstanding efforts have made this experiment possible. We thank the engineers and technicians for their work in constructing and maintaining the H1 detector, our funding agencies for financial support, the DESY technical staff for continual assistance and the DESY directorate for support and for the hospitality which they extend to the non DESY members of the collaboration. Furthermore, we thank Zoltan Nagy, Klaus Rabbertz and Markus Wobisch for fruitful discussions.

# References


[1] H1 and ZEUS Collaborations, "QCD analysis with determination of $\alpha_s$ based on HERA inclusive and jet data," *preliminary result: H1prelim-11-034, ZEUS-prel-11-001* (2011) .

[2] H1 Collaboration, C. Adloff *et al.*, "Measurement and QCD analysis of jet cross sections in deep-inelastic positron proton collisions at $\sqrt{s}$ of 300 GeV," *Eur. Phys. J. C* **19** (2001) 289.

[3] H1 Collaboration, F. D. Aaron *et al.*, "Jet production in $ep$ collisions at high $Q^2$ and determination of $\alpha_s$," *Eur. Phys. J. C* **65** (2010) 363.

[4] H1 Collaboration, A. Aktas *et al.*, "Measurement of inclusive jet production in deep-inelastic scattering at high $Q^2$ and determination of the strong coupling," *Phys. Lett. B* **653** (2007) 134.

[5] U. Bassler and G. Bernardi, "On the kinematic reconstruction of deep inelastic scattering at hera," *Nucl. Instr. and Meth. A* **361** (1995) 197.

[6] S. D. Ellis and D. E. Soper, "Successive combination jet algorithm for hadron collisions," *Phys. Rev. D* **48** (1993) 3160.

[7] M. Cacciari and G. P. Salam, "Dispelling the $N^3$ myth for the $k_T$ jet-finder," *Phys. Lett. B* **641** (2006) 57.

[8] S. Frixione and G. Ridolfi, "Jet photoproduction at HERA," *Nucl. Phys.* **B507** (1997) 315.

[9] K. Charchula, G. Schuler, and H. Spiesberger, "Combined QED and QCD radiative effects in deep inelastic lepton-proton scattering: The Monte Carlo generator DJANGO6," *Comput. Phys. Commun.* **81** (1994) 381.

[10] L. Lönnblad, "Ariadne version 4 – A program for simulation of QDC cascades implementing the colour dipole model," *Comput. Phys. Commun.* **71** (1992) 15.

[11] H. Jung, "Hard diffractive scattering in high energy $ep$ collisions and the Monte Carlo generator RAPGAP," *Comput. Phys. Commun.* **86** (1995) 147.

[12] B. Andersson, G. Gustafson, G. Ingelman, *et al.*, "Parton fragmentation and string dynamics," *Phys. Rep.* **97** (1983) 31.

[13] R. Brun, F. Bruyant, M. Maire, *et al.*, "GEANT: Simulation Program for Particle Physics Experiments. User Guide and Reference Manual," *CERN-DD/EE 84-1* (1987) .

[14] G. Grindhammer, M. Rudowicz, and S. Peters, "The fast simulation of electromagnetic and hadronic showers," *Nucl. Instr. and Meth. A* **290** (1990) 469–488.

[15] G. Grindhammer and S. Peters, "The parameterized simulation of electromagnetic showers in homogeneous and sampling calorimeters," *arXiv:hep-ex/0001020* (2000) .

[16] M. Ellerbrock, J. Marks, C. Risler, *et al.*, "Improved description of electromagnetic showers in h1fast," *H1-IN-617* (2005) .

[17] M. Ellerbrock, J. Marks, and C. Schwanenberger, “Description of hadronic showers in the optimized version of h1fast,” *H1-IN-623* (2005) .

[18] R. Kogler, *Measurement of jet production in deep-inelastic $ep$ scattering at HERA*. PhD thesis, Universität Hamburg, DESY-THESIS-2011-003, MPP-2010-175, 2011.

[19] A. Kwiatkowski, H. Spiesberger, and H. J. Möhring, “Heracles: an event generator for ep interactions at hera energies including radiative processes,” *Comput. Phys. Commun.* **69** (1992) 155–172.

[20] G. Ingelman, A. Edin, and J. Rathsman, “Lepto 6.5–a monte carlo generator for deep inelastic lepton-nucleon scattering,” *Comput. Phys. Commun.* **101** (1997) 108–134.

[21] H1 Collaboration, I Abt *et al.*, “The h1 detector at hera,” *Nucl. Instr. and Meth. A* **386** (1997) 310.

[22] B. Webber, “Factorization and jet clustering algorithms for deep-inelastic scattering,” *J. Phys. G* **19** (1993) 1567.

[23] Z. Nagy and Z. Trocsanyi, “Next-to-leading order calculation of four-jet observables in electron-positron annihilation,” *Phys. Rev. D* **59** (1999) 14020.

[24] Z. Nagy and Z. Trocsanyi, “Multijet Cross Sections in Deep Inelastic Scattering at Next-to-Leading Order,” *Phys. Rev. Lett.* **87** (2001) 82001.

[25] H1 and ZEUS Collaborations, “PDF fits including HERA-II high $Q^2$ data,” *preliminary result: H1prelim-10-142, ZEUS-prel-10-018* (2010) .

[26] ZEUS Collaboration, H. Abramowicz *et al.*, “Inclusive dijet cross sections in neutral current deep inelastic scattering at HERA,” *Eur. Phys. J. C* **70** (2010) 965.

[27] H.-L. Lai, M. Guzzi, J. Huston, *et al.*, “New parton distributions for collider physics,” *Phys. Rev. D* **82** (2010) 074024.

[28] NNPDF Collaboration, R. D. Ball *et al.*, “A first unbiased global NLO determination of parton distributions and their uncertainties,” *Nucl. Phys. B* **838** (2010) 136.

[29] T. Kluge, K. Rabbertz, and M. Wobisch, “FastNLO: Fast pQCD calculations for PDF fits,” `arXiv:hep-ph/0609285 [hep-ph]`.

[30] M. Botje, “A QCD analysis of HERA and fixed target structure function data,” *Eur. Phys. J. C* **14** (2000) 285.

[31] V. Barone, C. Pascaud, and F. Zomer, “A New global analysis of deep inelastic scattering data,” *Eur. Phys. J. C* **12** (2000) 243.

[32] H1 Collaboration, C. Adloff *et al.*, “Search for compositeness, leptoquarks and large extra dimensions in $eq$ contact interactions at HERA,” *Phys. Lett. B* **479** (2000) 358.

[33] H1 Collaboration, C. Adloff *et al.*, “Measurement and QCD analysis of neutral and charged current cross-sections at HERA,” *Eur. Phys. J. C* **30** (2003) 1.

[34] A. Martin, W. Stirling, R. Thorne, *et al.*, "Parton distributions for the LHC," *Eur. Phys. J. C* **63** (2009) 189.

[35] H1 Collaboration, F. D. Aaron, C. Alexa, V. Andreev, *et al.*, "Jet production in $ep$ collisions at low $Q^2$ and determination of $\alpha_s$," *Eur. Phys. J. C* **67** (2010) 1.

[36] S. Bethke, "The 2009 world average of $\alpha_s$," *Eur. Phys. J. C* **64** (2009) 689.

<table>
<tr><td>NC DIS Selection</td><td colspan="3">$150 < Q^2 < 15000\,\mathrm{GeV}^2 \quad 0.2 < y < 0.7$</td></tr>
<tr><td>Inclusive jet</td><td>$7 < P_\mathrm{T} < 50\,\mathrm{GeV}$</td><td></td><td rowspan="3">$-1.0 < \eta_\mathrm{lab} < 2.5$</td></tr>
<tr><td>Dijet</td><td>$5 < P_\mathrm{T}^\mathrm{jet1},\ P_\mathrm{T}^\mathrm{jet2} < 50\,\mathrm{GeV}$</td><td rowspan="2">$M_{12} > 16\,\mathrm{GeV}$</td></tr>
<tr><td>Trijet</td><td>$5 < P_\mathrm{T}^\mathrm{jet1},\ P_\mathrm{T}^\mathrm{jet2},\ P_\mathrm{T}^\mathrm{jet3} < 50\,\mathrm{GeV}$</td></tr>
</table>

Table 1: Selection criteria for the NC DIS and jet samples.

| Bin number | $Q^2$ range (in $\mathrm{GeV}^2$) |
|---|---|
| 1 | $150 \leq Q^2 < 200$ |
| 2 | $200 \leq Q^2 < 270$ |
| 3 | $270 \leq Q^2 < 400$ |
| 4 | $400 \leq Q^2 < 700$ |
| 5 | $700 \leq Q^2 < 5000$ |
| 6 | $5000 \leq Q^2 < 15000$ |

| Bin label | $P_\mathrm{T}$ or $\langle P_\mathrm{T}\rangle$ range (in GeV) |
|---|---|
| $\alpha$ | $7 \leq P_\mathrm{T} < 11$ |
| $\beta$ | $11 \leq P_\mathrm{T} < 18$ |
| $\gamma$ | $18 \leq P_\mathrm{T} < 30$ |
| $\delta$ | $30 \leq P_\mathrm{T} < 50$ |

| Bin label | Dijet $\xi$ range |
|---|---|
| a | $0.006 \leq \xi < 0.02$ |
| b | $0.020 \leq \xi < 0.04$ |
| c | $0.040 \leq \xi < 0.08$ |
| d | $0.080 \leq \xi < 0.316$ |

| Bin label | Trijet $\xi$ range |
|---|---|
| A | $0.01 \leq \xi < 0.04$ |
| B | $0.04 \leq \xi < 0.08$ |
| C | $0.08 \leq \xi < 0.50$ |

Table 2: The bins in $Q^2$, $P_\mathrm{T}$ or $\langle P_\mathrm{T}\rangle$ for inclusive jets, dijets and trijets as shown in the following figures. For dijets and trijets also the bins in $\xi$ are shown.

| Measurement | $\alpha_S(M_Z)$ | Uncertainty | | | $\chi^2/\mathrm{ndf}$ |
|---|---|---|---|---|---|
| | | experimental | theory | PDF | |
| inclusive jet | 0.1190 | 0.0021 | $^{+0.0050}_{-0.0056}$ | 0.0020 | 30.2/23 |
| dijet | 0.1146 | 0.0022 | $^{+0.0044}_{-0.0045}$ | 0.0021 | 25.5/23 |
| trijet | 0.1196 | 0.0016 | $^{+0.0055}_{-0.0039}$ | 0.0010 | 18.6/17 |

Table 3: Values of $\alpha_s(M_Z)$ obtained from fits to the individual inclusive jet, dijet and trijet cross sections. The fitted values are given with their experimental, theoretical and PDF uncertainties and the normalised $\chi^2$ of the fit.

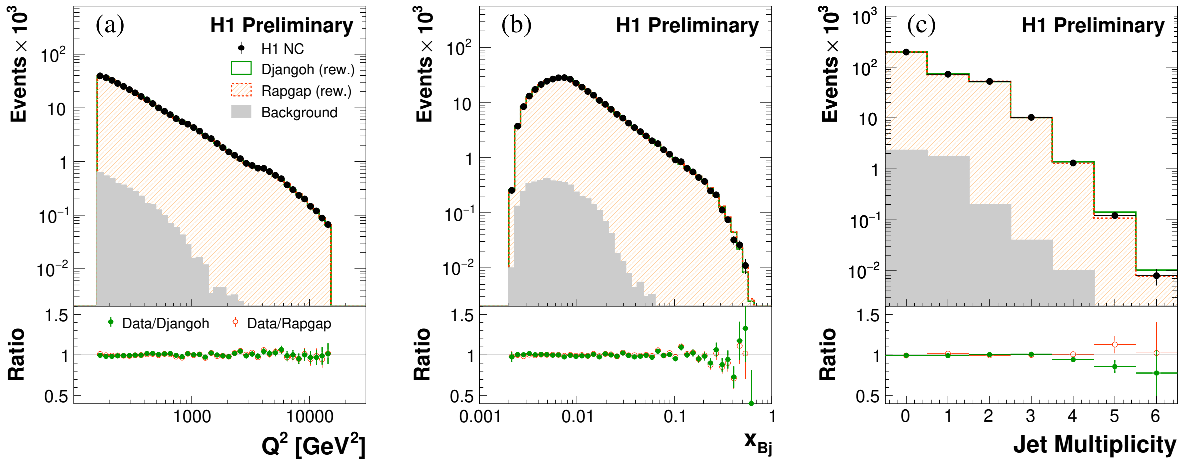


Figure 1: Distribution of the selected events for the NC DIS sample shown as a function of the virtuality $Q^2$ (a), the Bjorken scaling variable $x_{\mathrm{Bj}}$ (b) and the jet multiplicity (c). The data are compared with weighted MC simulations, DJANGOH (green) and RAPGAP (red, dashed area). The background, which consists mainly of QED Compton and photoproduction events, is shown as shaded grey area.

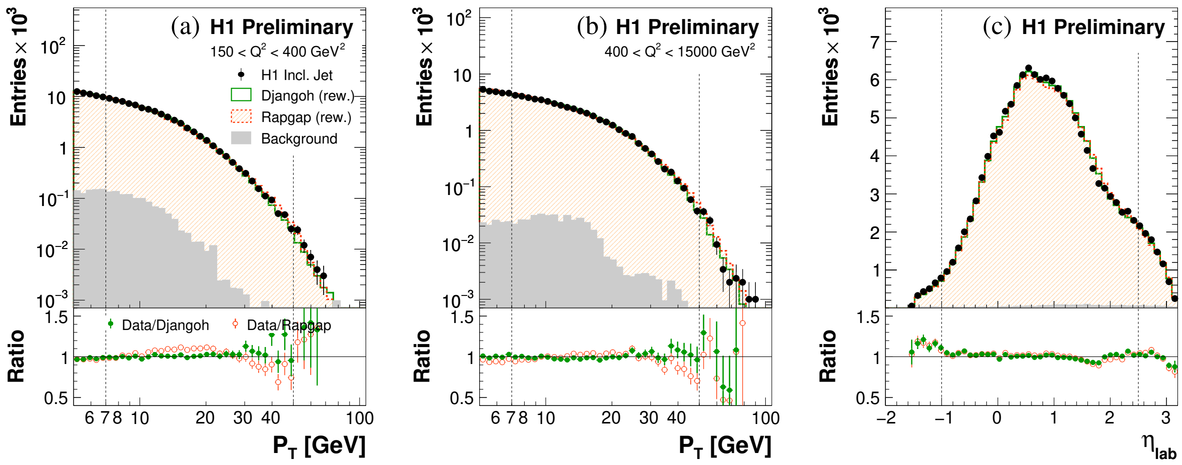


Figure 2: Transverse momentum distributions of jets in the Breit frame for the inclusive jet sample at low (a) and high $Q^2$ (b) and pseudorapidity distribution of jets boosted back into the laboratory frame (c). The data are compared with weighted MC simulations, DJANGOH (green) and RAPGAP (red, dashed area). The background, which consists mainly of QED Compton and photoproduction events, is shown as shaded grey area.

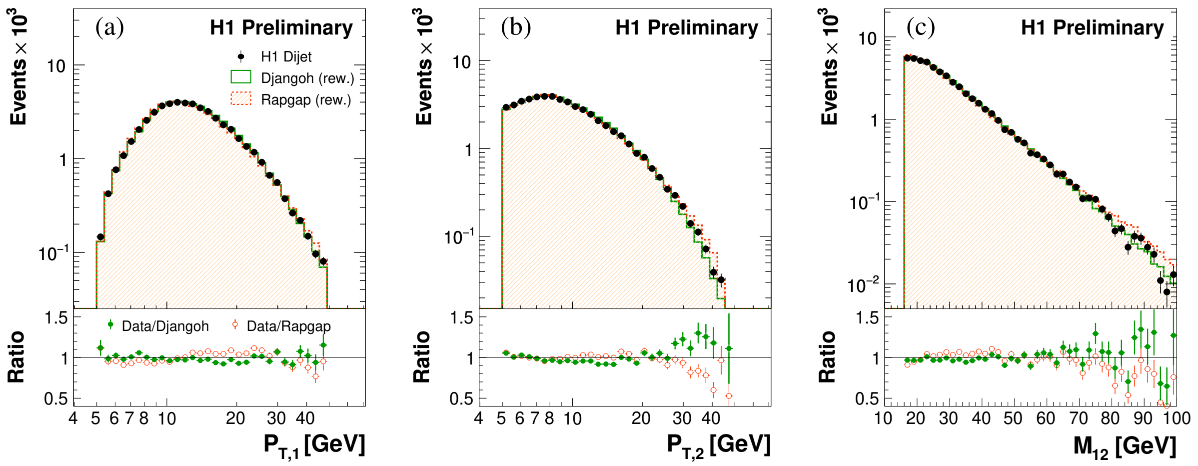


Figure 3: Transverse momentum distributions of jets in the Breit frame (a) and (b) and dijet invariant mass (c) for the dijet sample. The data are compared with weighted MC simulations, DJANGOH (green) and RAPGAP (red, dashed area).

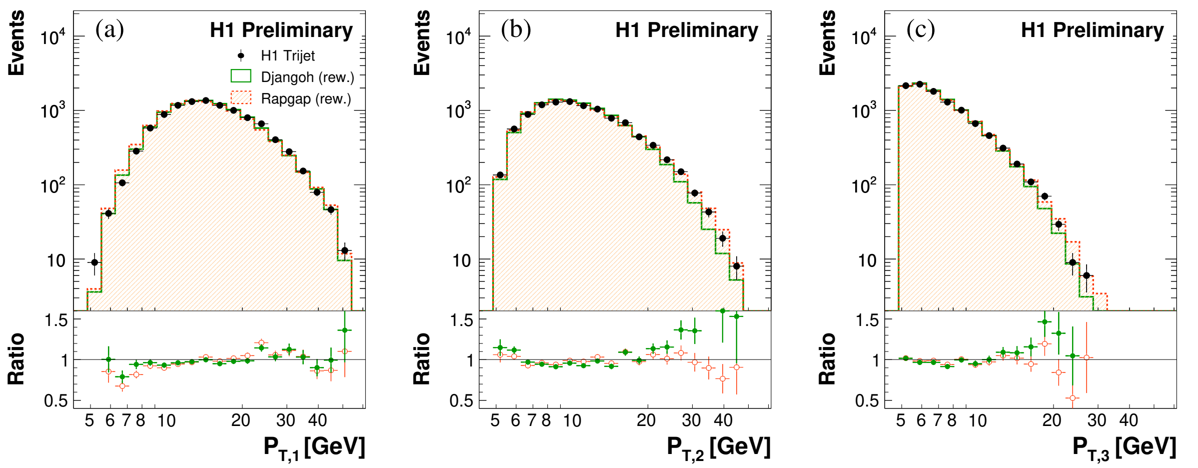


Figure 4: Transverse momentum distributions of jets in the Breit frame (a), (b) and (c) for the trijet sample. The data are compared with weighted MC simulations, DJANGOH (green) and RAPGAP (red, dashed area).

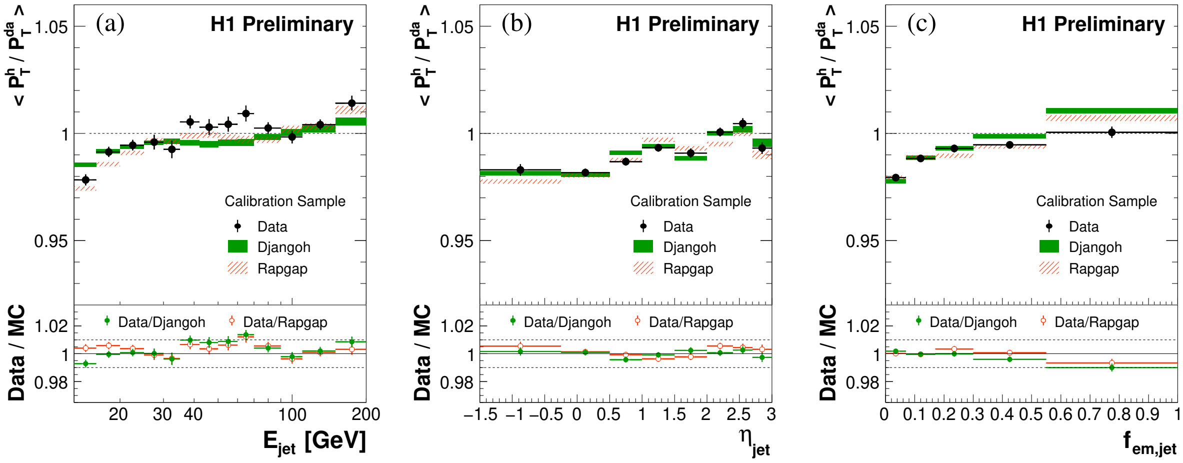


Figure 5: Ratio of the calibrated transverse momentum of the hadronic final state $P_{\mathrm{T}}^{\mathrm{h}}$ to the reference measurement $P_{\mathrm{T}}^{\mathrm{da}}$ as function of the jet energy (a), jet pseudorapidity (b) and the electromagnetic energy fraction of the jet (c). The double-ratio of data to MC is shown at the bottom of each plot.

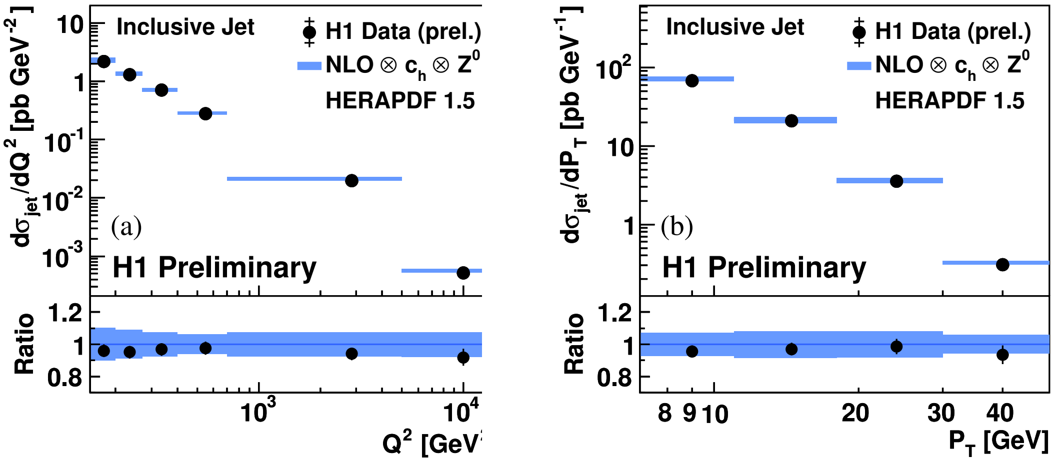


Figure 6: The inclusive jet cross sections in NC DIS measured as a function of $Q^2$ (a) and the transverse momentum $P_{\mathrm{T}}$ in the Breit frame (b). The measurements refer to the phase-space given in table 1. The inner error bars represent the statistical uncertainty. The outer error bars show the total experimental uncertainties, defined as the quadratic sum of the statistical and systematic uncertainties. The NLO QCD predictions, with parameters described in section 5 and corrected for hadronisation effects are shown together with the theory uncertainties associated with the renormalisation and factorisation scales and the hadronisation (blue band). The ratio of data with respect to the NLO QCD prediction is shown in the lower part of each plot.

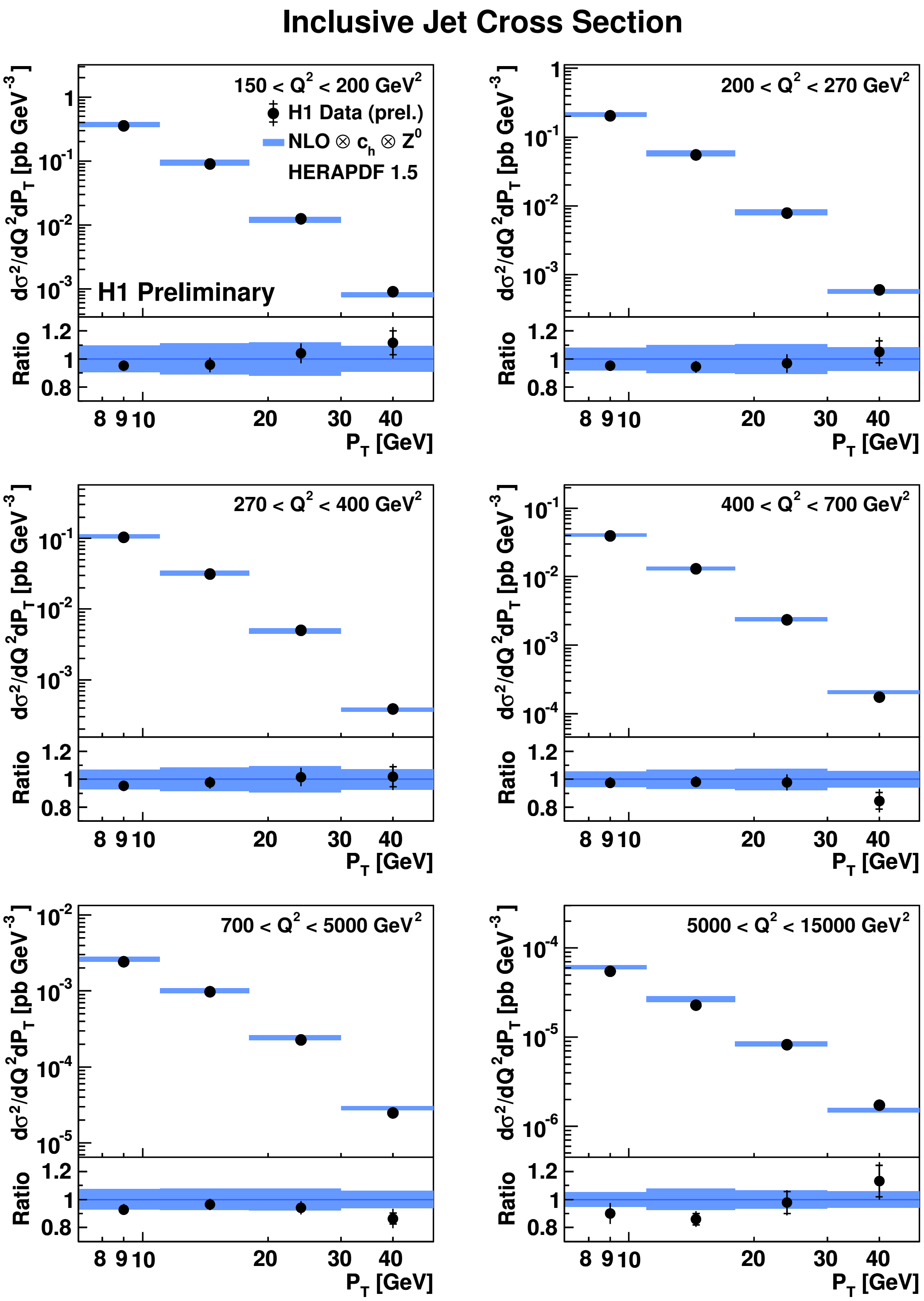


Figure 7: The inclusive jet cross sections in NC DIS measured as a function of the jet transverse momentum $P_{\mathrm{T}}$ in the Breit frame in regions of $Q^2$. The measurements refer to the phase-space given in table 1, and other details are given in the caption to figure 6.

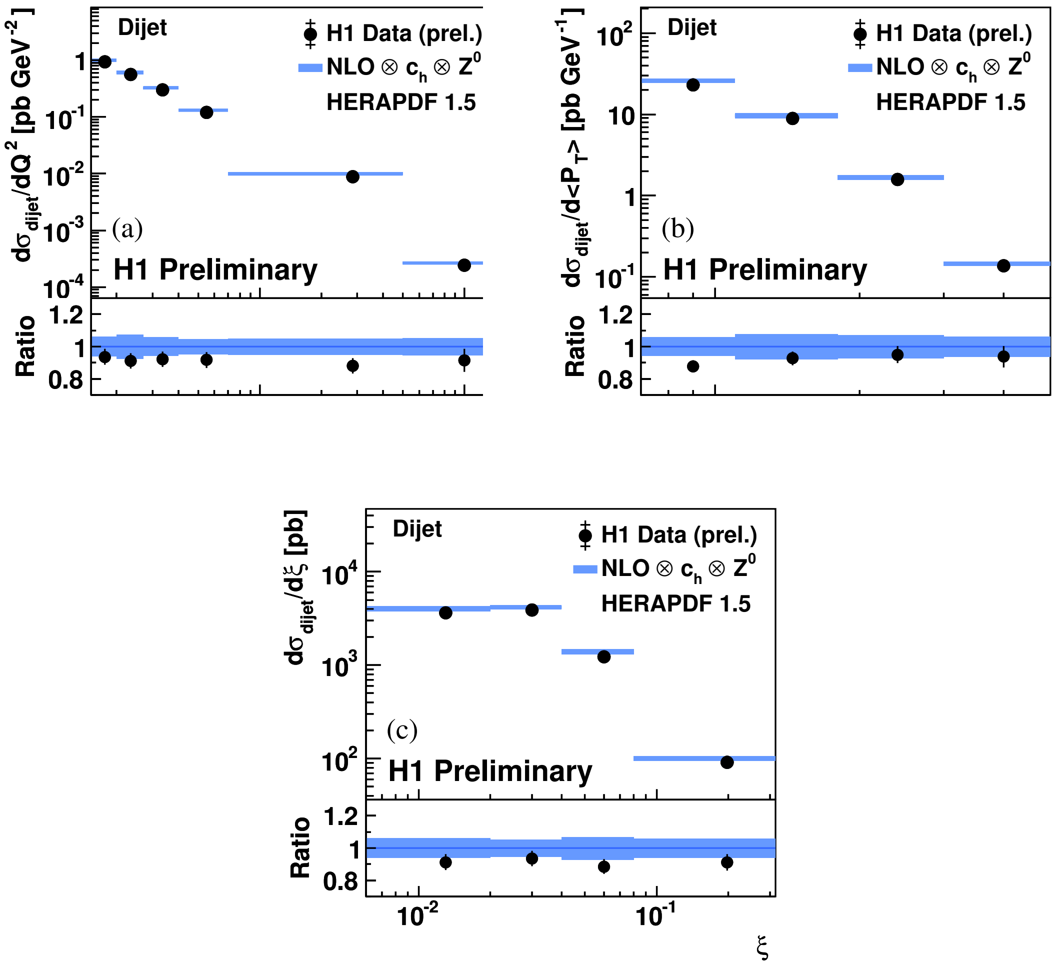


Figure 8: The dijet cross sections in NC DIS measured as a function of $Q^2$ (a), the mean transverse momentum of the two leading jets $\langle P_{\mathrm{T}} \rangle$ in the Breit frame (b) and the proton momentum fraction $\xi$ (c). The measurements refer to the phase-space given in table 1, and other details are given in the caption to figure 6.

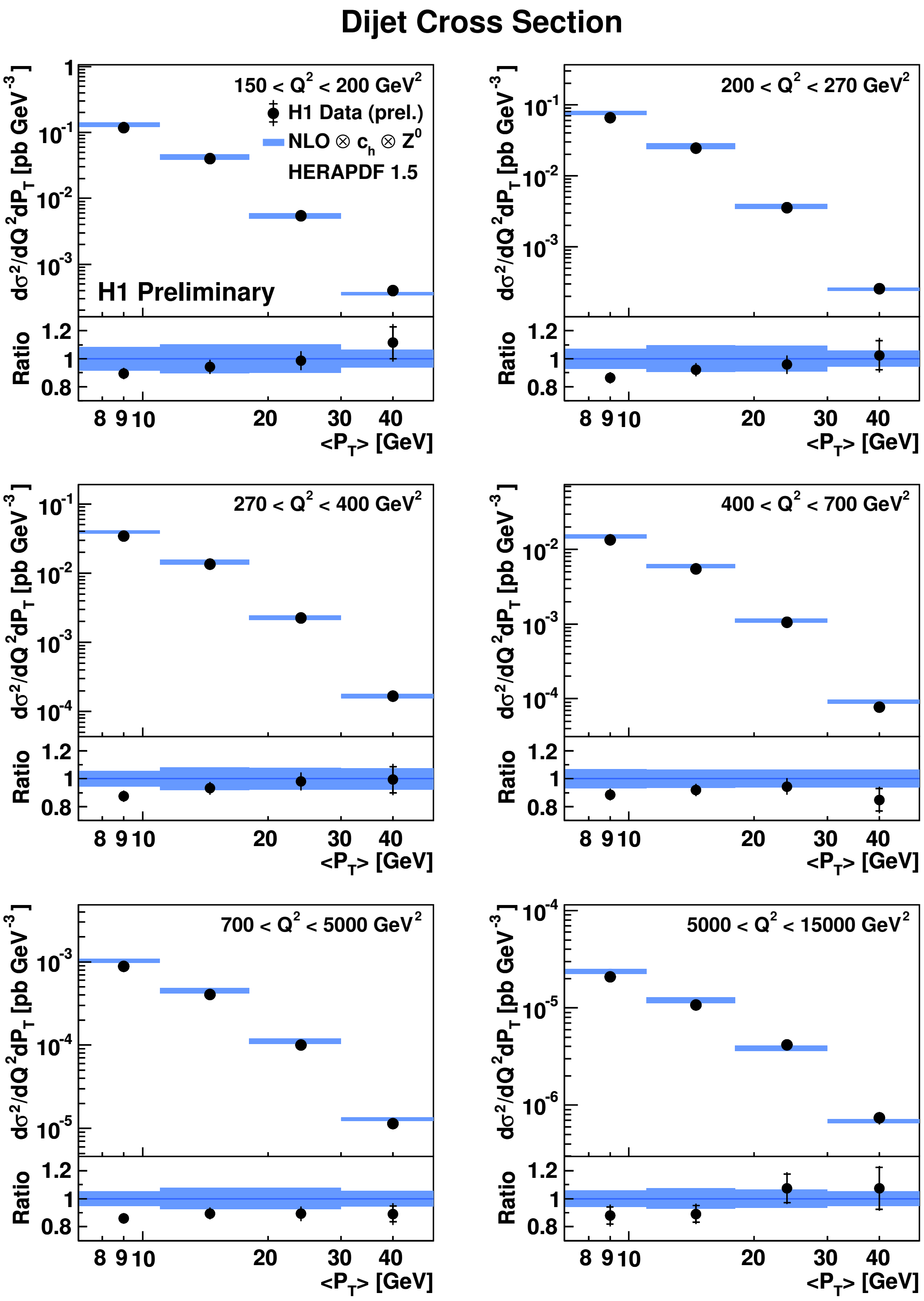


Figure 9: The dijet cross sections in NC DIS measured as a function of the average transverse momentum of the two leading jets $\langle P_{\mathrm{T}} \rangle$ in the Breit frame in regions of $Q^2$. The measurements refer to the phase-space given in table 1, and other details are given in the caption to figure 6.

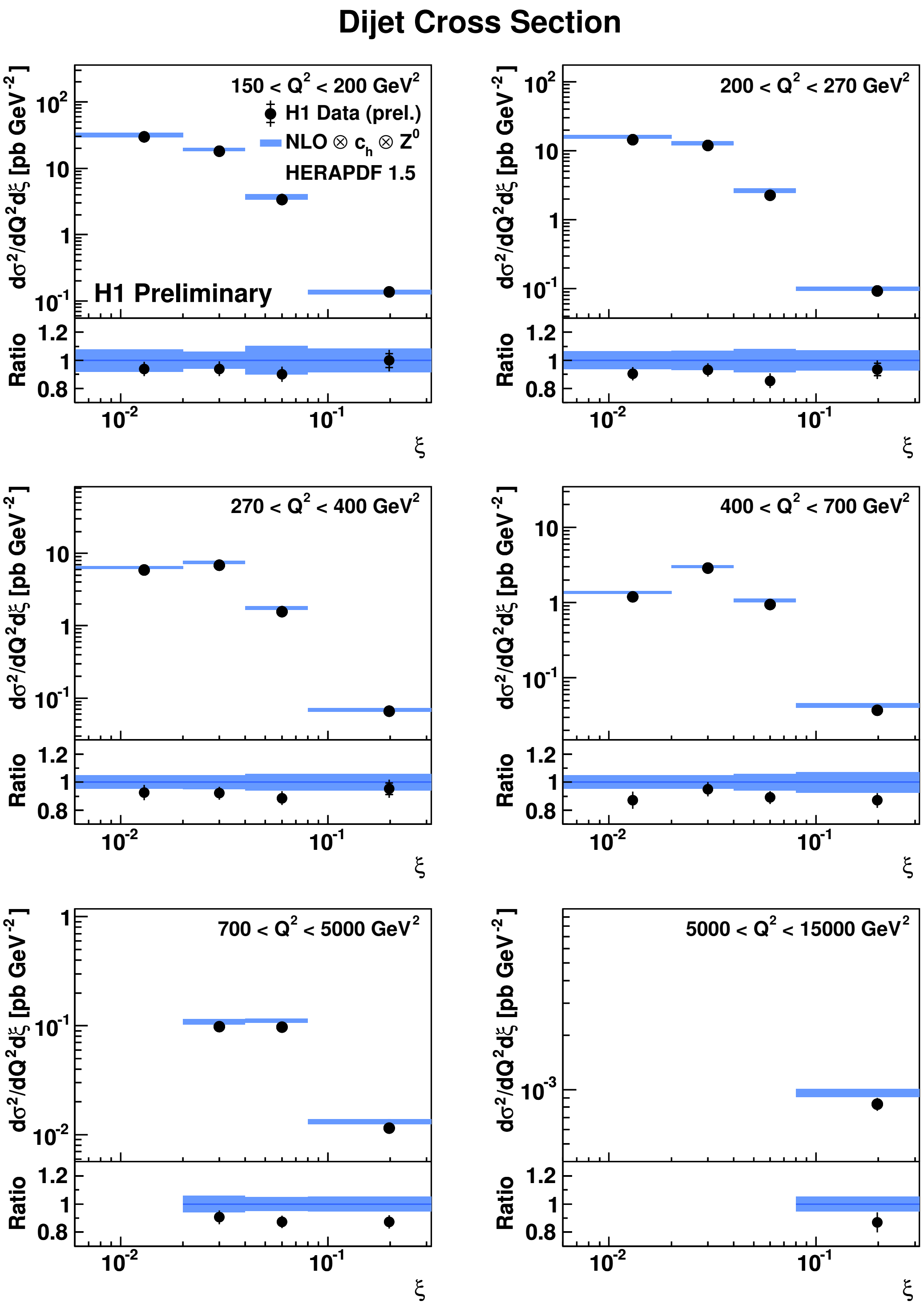


Figure 10: The dijet cross sections in NC DIS measured as a function of the proton momentum fraction $\xi$ in regions of $Q^2$. The measurements refer to the phase-space given in table 1, and other details are given in the caption to figure 6.

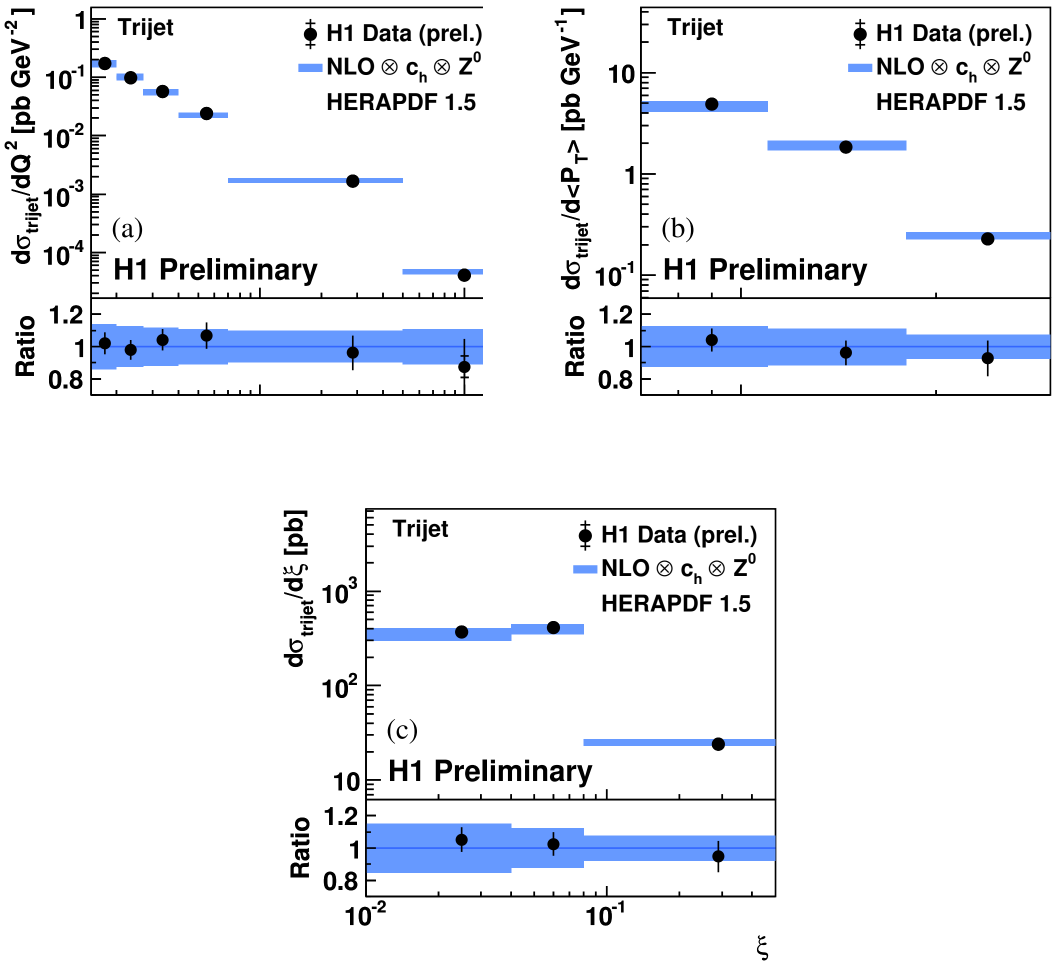


Figure 11: The trijet cross sections in NC DIS measured as a function of $Q^2$ (a), the mean transverse momentum of the three leading jets $\langle P_{\mathrm{T}} \rangle$ in the Breit frame (b) and the proton momentum fraction $\xi$ (c). The measurements refer to the phase-space given in table 1, and other details are given in the caption to figure 6.

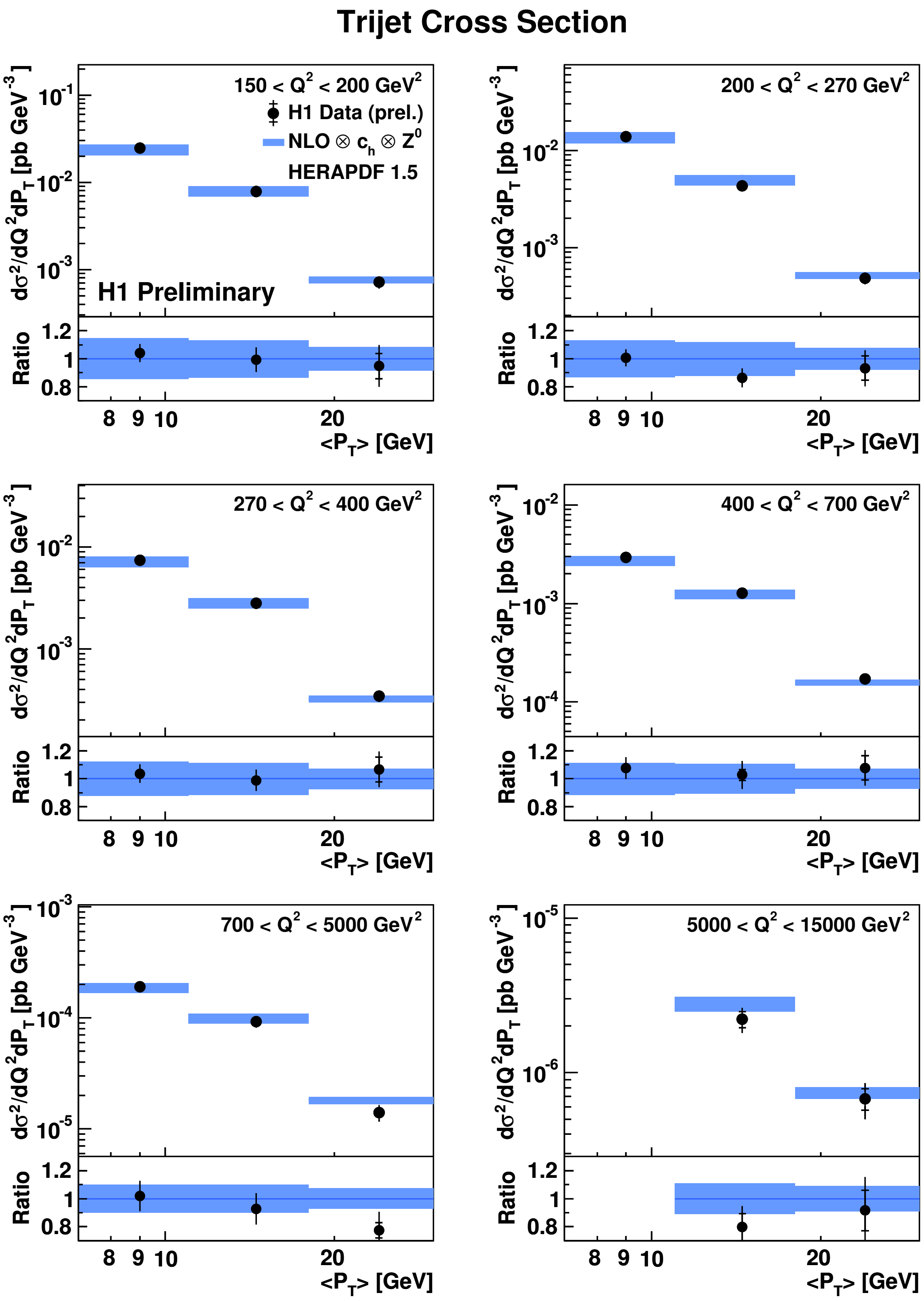


Figure 12: The trijet cross sections in NC DIS measured as a function of the average transverse momentum of the three leading jets $\langle P_{\mathrm{T}} \rangle$ in the Breit frame in regions of $Q^2$. The measurements refer to the phase-space given in table 1, and other details are given in the caption to figure 6.

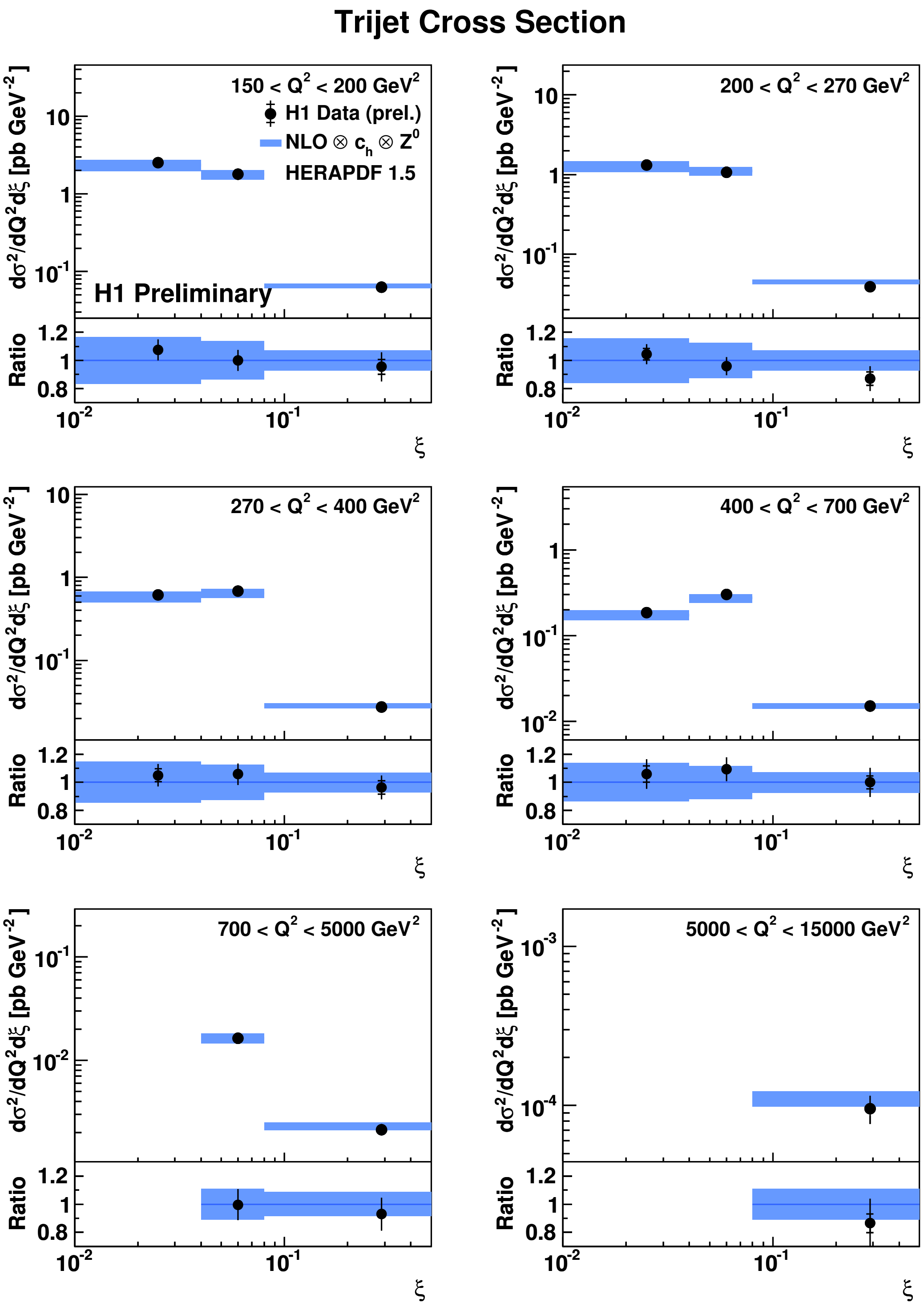


Figure 13: The trijet cross sections measured as a function of the proton momentum fraction $\xi$ in regions of $Q^2$. The measurements refer to the phase-space given in table 1, and other details are given in the caption to figure 6.

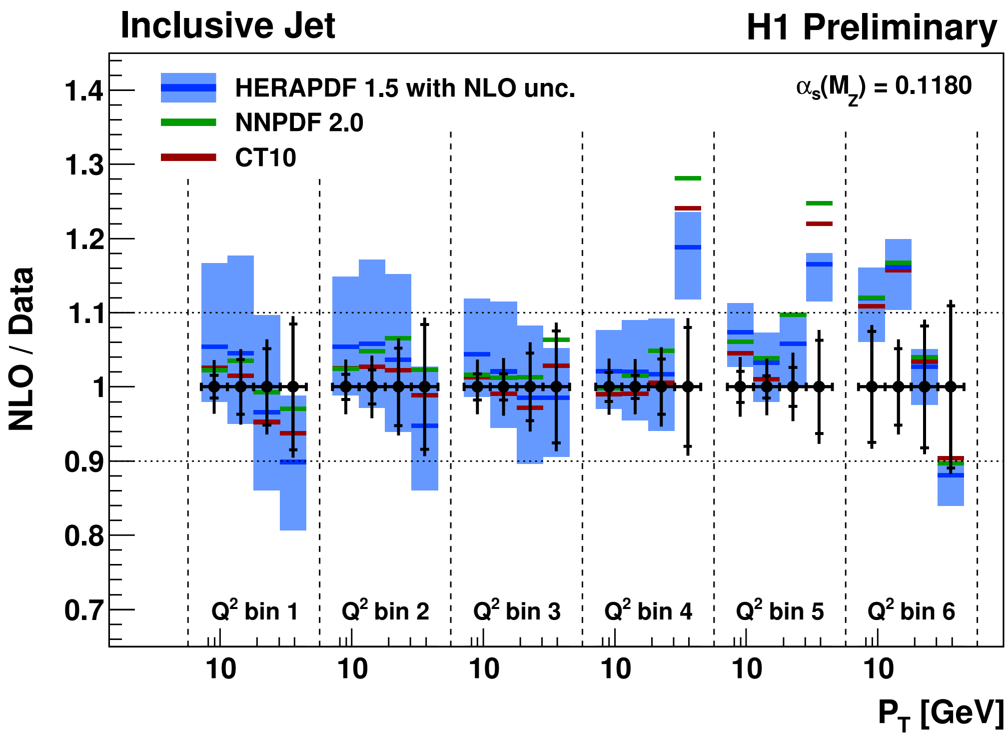


Figure 14: The ratio of NLO predictions for inclusive jet production in NC DIS using different PDF parametrisations to the inclusive jet cross sections as shown in figure 7. The ranges of the bins in $Q^2$ and $P_{\rm T}$ are given in table 2. The inner error bars denote the total uncorrelated experimental uncertainty, and the outer error bars show the full experimental uncertainty. The theoretical uncertainty due to variation of the renormalisation and factorisation scales is shown for the calculation with HERAPDF1.5 as blue band. For the two other calculations only the central values are shown.

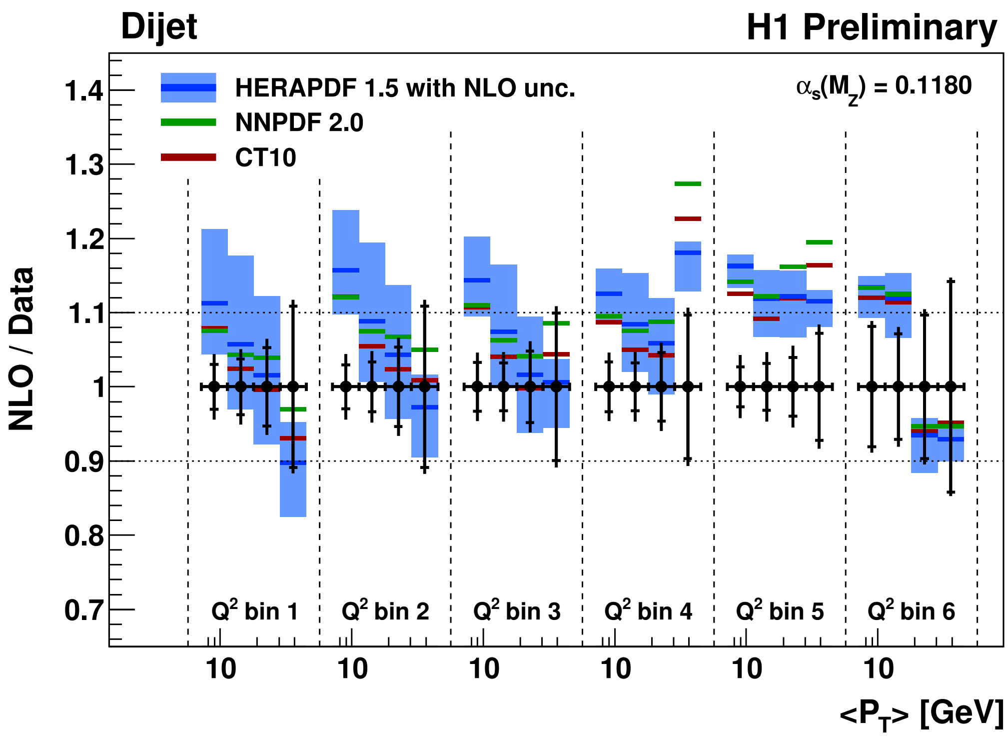


Figure 15: The ratio of NLO predictions for dijet production in NC DIS using different PDF parametrisations to the dijet cross sections as shown in figure 9. Other details are given in the caption to figure 14.

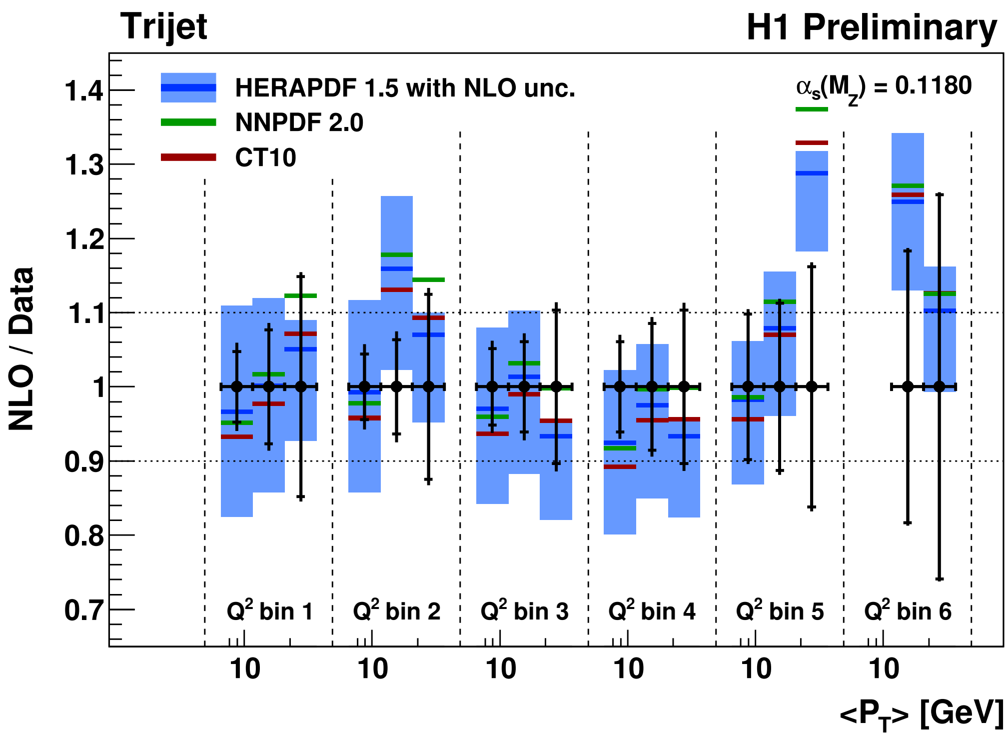


Figure 16: The ratio of NLO predictions for trijet production in NC DIS using different PDF parametrisations to the trijet cross sections as shown in figure 12. Other details are given in the caption to figure 14.

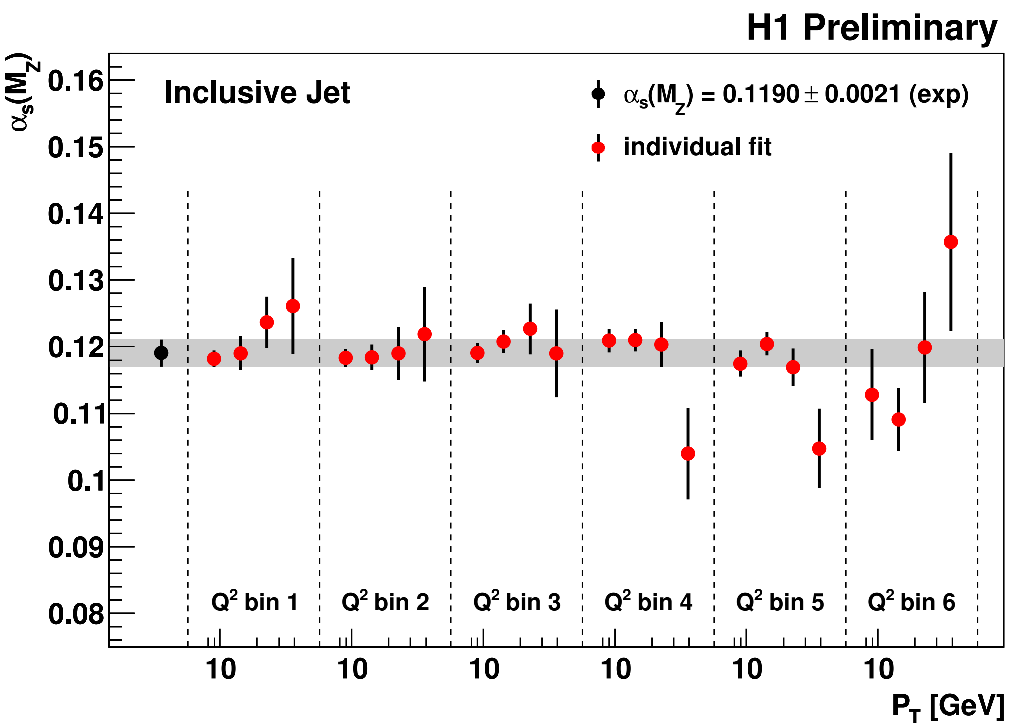


Figure 17: Values of $\alpha_s(M_Z)$ determined using the inclusive jet cross sections measured in 24 bins of $Q^2$ and $P_{\mathrm{T}}$. Each value of $\alpha_s(M_Z)$ is obtained by an individual fit to each cross section point and shown in red. The error bars denote the uncertainty on $\alpha_s(M_Z)$ due to the total uncorrelated experimental uncertainty of each data point. The central value obtained from the fit to all 24 bins is shown in black, with the total experimental uncertainty shown as grey band.

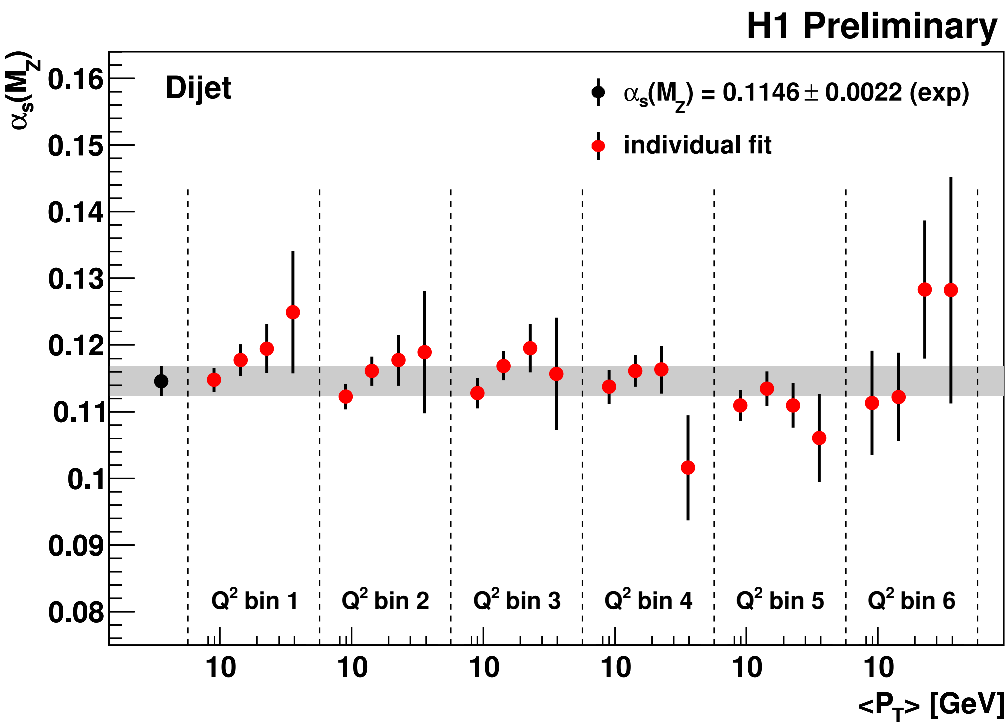


Figure 18: Values of $\alpha_s(M_Z)$ determined using the dijet cross sections measured in $24$ bins of $Q^2$ and $\langle P_{\rm T}\rangle$. Other details are given in the caption to figure 17.

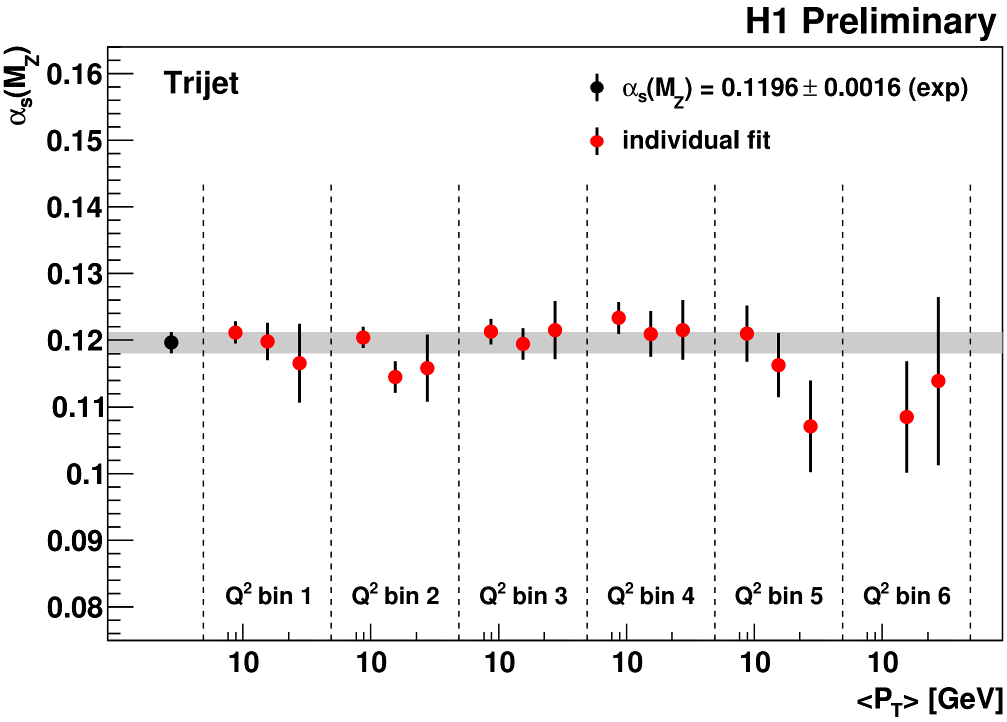


Figure 19: Values of $\alpha_s(M_Z)$ determined using the trijet cross sections measured in 17 bins of $Q^2$ and $\langle P_{\rm T}\rangle$. Other details are given in the caption to figure 17.